Journal Pre-proof

Liquid phase assisted synthesis of (Ti,V,Nb,Ta,W)C-Ni high entropy carbide cermets by conventional pressureless sintering

Zahid Anwer, Shuigen Huang, Jozef Vleugels

Please cite this article as: Z. Anwer, S. Huang and J. Vleugels, Liquid phase assisted synthesis of (Ti,V,Nb,Ta,W)C-Ni high entropy carbide cermets by conventional pressureless sintering, *International Journal of Refractory Metals and Hard Materials* (2021), https://doi.org/10.1016/j.ijrmhm.2022.105914

This is a PDF file of an article that has undergone enhancements after acceptance, such as the addition of a cover page and metadata, and formatting for readability, but it is not yet the definitive version of record. This version will undergo additional copyediting, typesetting and review before it is published in its final form, but we are providing this version to give early visibility of the article. Please note that, during the production process, errors may be discovered which could affect the content, and all legal disclaimers that apply to the journal pertain.

Liquid phase assisted synthesis of (Ti,V,Nb,Ta,W)C-Ni high entropy carbide cermets by conventional pressureless sintering

Zahid Anwer[*a], Shuigen Huang[a], Jozef Vleugels[a]

[a]*Department of Materials Engineering, KU Leuven, Kasteelpark Arenberg 44, box 2450 - 3001 Leuven, Belgium.*

[*] Corresponding author
E-mail address: zahid.anwer@kuleuven.be or imzahidanwer@gmail.com

Abstract

Two-phase fully dense high entropy carbide (HEC) cermets were successfully prepared following the conventional cemented carbide/cermet processing route. Cold isostatically pressed equimolar TiC, VC, NbC, TaC and WC powder mixtures with 12 vol.% Ni binder were pressureless sintered in the solid state and liquid phase sintering regimes respectively. A homogeneous rock-salt (space group $Fm\bar{3}m$) HEC phase embedded in a nickel alloy binder was attained by liquid phase sintering at 1420°C. Thermodynamic simulations were conducted to predict the equilibrium phases and carbide/binder phase contents. The phase evolution was investigated at seven different sintering temperatures in the 900-1420°C window. Thermogravimetry and differential scanning calorimetry analysis were performed to follow up the sintering process. Electron probe microanalysis was used to map the elemental distribution as well as to quantify the constituent phase contents. Nanoindentation were performed to correlate the difference in mechanical properties of the core-rim structured HEC grains with the chemical composition. The liquid phase sintered (Ti,V,Nb,Ta,W)C- 12 vol.% Ni had a Vickers hardness of 14.3 GPa and Palmqvist indentation fracture toughness of 9.2 MPa. m$^{1/2}$.

Keywords : High Entropy Carbides, Cermets, Pressureless Sintering, Microstructure, Nanoindentation

1. Introduction

The transition-metal carbides from group IV, V & VI elements possess the highest melting point and are recognized as the hardest among all known compounds [1–3]. In cemented carbides and cermets, compounds such as WC, TiC, Ti(C,N), (W,Ti,Ta,Nb)C, etc. form in combination with a soft metal binder (Co, Ni, Fe, Ni-Co, etc.) a ceramic-metal composite which gives an optimum combination of hardness, strength and toughness, suitable for cutting tools and other wear-resistant components [2,4–6]. However, due to health and supply risk reasons of WC and Co, serious efforts at academic and industrial level have been directed towards finding alternative materials for cutting and wear-resistance applications [6–10]. Alternatively, TiC-TiN-WC-Mo-Ni and (Ti,Mo,W,V)(C,N)-Ni,Co type cermets were also developed to partially replace WC-Co for cutting tools, which due to their lower fracture toughness and strength are limited to high-speed finishing operations [11].

The recent discovery of high entropy alloys (HEA) has attracted a multitude of researchers to assess the feasibility of using HEA as binders in cemented carbides and cermets [9]. In the pioneering work, C. Chen *et al.* [12] reported the novel WC-Al$_{0.5}$CoCrCuFeNi which had a higher hot hardness and fracture toughness than commercially available WC-Co. Recently, E. Holmström *et al.* [13] developed a new cutting tool using a CoCrFeNi binder and WC hard phase. This new WC-HEA outperformed current state-of-the-art WC-Co by demonstrating a higher resistance to plastic deformation at higher cutting speeds. In a comprehensive review, J.M. Torralba *et al.* [9] reported on the Vickers hardness (HV) vs. fracture toughness (K$_{1c}$) relationship of Co and HEA based cemented carbides/cermets and showed how competitive they are to conventional cemented carbides [9]. The concept of HEA also inspired the development of novel high entropy ceramics such as high entropy oxides [14], borides [15], carbides [16–19], dual phase carbide and boride [20], nitrides [21], carbonitrides [22], oxides [23] and fluorides [24].

In comparison to mono or binary carbides, high entropy carbides (HEC) have demonstrated higher hardness and elastic modulus as well as good oxidation, corrosion, and wear resistance [16,18,25–27]. Therefore, HEC have attracted considerable attention as potential material for demanding applications such as aerospace vehicles, cutting tools, rocket nozzles, nuclear reactors, etc. [25,26]. Although this new class of multi-element components have shown great promise, the exploration of the vast compositional space is the biggest challenge [25]. In this regard, torch carrying work has been carried out by P. Sarker *et al.* [18] who developed an *ab initio* entropy descriptor to calculate the entropy forming ability EFA (eV/atom^{-1}) of 56 five-metal carbide compositions comprising of Ti, Zr, Hf, V, Nb, Ta, Mo and W. Based on their EFA values, only 9 compositions were synthesized out of which only 6 compositions (EFA ≥ 50 eV/atom^{-1}) formed a single phase solid solution. The choice of five principle metal elements was inherited from the original high entropy alloys theory. According to this theory, systems having five or more components mixed in equal or near equimolar ratios, possess molar configuration entropy S ≥ 1.61R (with R the universal gas constant). These multi-component systems are stabilized into a single phase homogeneous crystalline structure by virtue of entropy [29]. Following the work of P. Sarker *et al.* [18], X. Yan *et al.* [17] synthesized bulk (Hf$_{0.2}$Zr$_{0.2}$Ta$_{0.2}$Nb$_{0.2}$Ti$_{0.2}$)C single phase high entropy ceramics (EFA = 100 eV/atom^{-1}) which showed low thermal conductivity and high mechanical properties. D. Sangiovanni *et al.* [30] utilized a fundamental design approach of using the valence electron concentration (VEC) and demonstrated this approach on two

five-metal high entropy carbide systems (Mo,Nb,Ta,V,W)C (VEC = 9.4 e⁻/f.u.) and (Hf,Ta,Ti,W,Zr)C (VEC = 8.6 e⁻/f.u.) respectively. They demonstrated that HECs with a VEC ≥ 9.5 e⁻/formula unit showed enhanced plasticity and a single-phase rock salt crystal structure.

Recently, J. Pötschke *et al.* [31] successfully synthesized two HEC based cermets, i.e. (Hf,Ta,Ti,Nb,V)C-19.2 vol.% Co and (Ta,Ti,Nb,V,W)C-19.2 vol.% Co, using gas pressure sintering (100 bar Ar) of milled HEC-Co powder mixtures at 1400°C. The reported EFA values for these two HEC systems are 100 eV/atom⁻¹ [18] and 77 eV/atom⁻¹ [18], respectively. However, the authors reported splitting up of (Hf,Ta,Ti,Nb,V)C phase into two similar HEC phases with some remnant TaC, HfO₂ and clustered vanadium titanium carbide phases, whereas the (Ta,Ti,Nb,V,W)C grains remained intact. Inspired by the initial work of E. Castle *et al.* and J. Dusza *et al.* [16,19], HEC based (Zr,Hf,Nb,Ta)C-xCo (x= 5, 10, 20 wt.%) cermets comprising four-metal carbides have been reported by X. Wang *et al.* [32]. So far, the synthesis of HEC powder is mainly done by mechanical alloying, self-propagating high-temperature synthesis (SHS), liquid precursor method, direct sintering of monocarbides, reaction sintering involving elemental powders or carbothermal reduction of metal oxides [27]. Among various sintering techniques, SPS and hot pressing are most commonly used with a typical sintering temperature of 1800°C [27].

In this work, a typical one-step cemented carbide processing strategy was applied to synthesize a two phase cubic (Ti,V,Nb,Ta,W)C-12 vol.% Ni cermet using liquid phase sintering. Thermodynamic simulations were used to calculate the pseudo-binary phase diagram and predict the equilibrium phases within the solid state and liquid phase sintering regimes. The microstructure and phase analysis was studied as function of sintering temperature and correlated with the measured mechanical properties.

Table 1. Characteristics of the starting powders as received from the suppliers.

2. Materials and Methods

Equimolar TiC-VC-NbC-TaC-WC mixtures with a fixed 12 vol.% Ni were prepared from commercially available powders, the details are given in Table 1. The weighed powder mixture was wet milled for 48 h in a polyethylene container with a 5:1 ball to powder ratio using WC-Co milling media on a multidirectional mixer (Turbula, WAB, Switzerland). The slurry was dried on a rotary evaporator at 78°C. The powder mixture was shaped into cylinders (15 mm diameter, 10 mm height) through cold isostatic pressing (EPSI, Belgium) at 200 MPa for 60 seconds. Pressureless sintering of the green compacts was carried out in an actively pumped vacuum (10-20 Pa) graphite furnace (HP, W100/150–2200-50 LAX, FCT Systeme, Frankenblick, Germany) at 900, 1050, 1200, 1300, 1360, 1390 or 1420°C for 90 min isothermal holding time. A heating rate of 20°C/min from room temperature up to 900 or 1050°C, and subsequently at 5°C/min up to 1250°C or 3°C/min up to 1360, 1390 and 1420°C was used.

Powders	Source	Particle size FSSS (µm)	C (wt.%)	O (wt.%)	wt.%	vol.%
NbC	CBMM, Brazil	1.75	10.80	0.29	15.2	19.1
TiC	H.C. Starck, Germany	1.0 – 1.5	19.60	1.00	8.7	17.3

VC	Changsha Langfeng Metal Materials Co. Ltd, China	3.38	18.08	0.32	9.1	15.4
WC	Umicore, CW5300, Belgium	1.7-2.3	6.14	0.08	28.4	17.6
TaC	CNMNC, TaC-1 type, Ningxia, China	≤ 1.0	6.20	0.25	28.0	18.9
Ni	Vale, T123TM, U.K	3.0 – 7.0	-	0.04	10.6	11.7

Thermodynamic simulations were carried out using Thermo-Calc version 2020b and database TCFE10 [33]. The post-sintering density of cermets was measured in demineralized water at room temperature according to the Archimedes method while the theoretical density of the HEC-cermet (9.80 g/cm^3) was calculated according to the rule of mixtures based on the starting powder composition [34]. The individual densities of NbC (4.4691 Å[3], 7.81 g/cm^3), TiC (4.3280 Å[3], 4.91 g/cm^3), VC (4.1590 Å[3], 5.6? g/cm^3), WC (15.8 g/cm^3[3]), TaC (4.4550 Å[3], 14.49 g/cm^3) and Ni (3.5239 Å[35], 8.91 g/cm^3) were calculated from their corresponding lattice parameters using Vegard's law [36]. The cermets were cut with a diamond saw (Metkon Servocut 301-AA-V-AX, Bursa, Turkey). Mirror-finished cross-sections were prepared on a semi-automatic grinding and polishing machine (LaboForce 100/LaboPol 30; Struers Copenhagen, Denmark) with 15, 3 and 1 um diamond suspensions and final polishing was carried out using colloidal silica. The porosity in the sintered cermets was determined according to ASTM Standard B276 / ISO-4505 by light optical microscopy at a 100 times magnification. The microstructures were observed by high resolution scanning electron microscopy (NanoSEM, Nova™ 450 FEGSEM, FEI, The Netherlands) and EBSD mapping was carried out at 20kV with 0.1 µm step size and the data were analysed using OIM analysis software. Electron Probe Micro Analysis (EPMA, JXA-8530F, JEOL Ltd, Japan) was used at 15 kV and 100 nA for WDS elemental mapping, quantitative analysis (ZAF correction method) and line analysis. The carbide grain size was estimated from at least 250 grains at 10,000 times magnification BSE-micrographs by the line intercept method using imageJ software [37]. Contiguity was determined according to the method proposed by C. Smith & L. Guttman [38]. Phase identification was carried out on a θ-θ X-ray diffractometer (XRD, Bruker D2 Phaser, Lynxeye) using Cu K$_\alpha$ radiation (30 kV, 10 mA). The diffraction patterns were obtained through a step scan mode (step size 0.02°, scan rate 0.1s/step) in the 30°- 80° 2θ range. The peak positions of carbide and binder phases were fitted with the Pseudo-Voigt function and the lattice parameters were refined using the Rietveld method in X'pert Highscore Plus software [39]. The mass loss during sintering was determined by simultaneous differential scanning calorimetry (DSC) and thermogravimetry analysis (TGA) (SDT Q600 T.A Instruments) at 1420°C with 10 min isothermal holding time under Argon gas, using a heating and cooling rate of 10°C/min. The carbon content of powder mixture and sintered cermets was measured by carbon combustion analysis at 1250°C (Ströhlein Coulomat 702 SO/CS) and the presented data are the arithmetic mean of three measurements. The Vickers hardness, HV$_{30}$, (FV-700, Future Tech Corp., Japan) was evaluated with an indentation load of 30 kg for 15 sec, and the Palmqvist indentation fracture toughness (K$_{1c}$) was measured from the radial crack lengths around the HV$_{30}$ indentations using the Shetty formula [40]. The values of five indentations are presented as mean and standard deviation. Nanoindentations (Nano hardness tester; CSM Instruments SA, Switzerland) were carried out with a Berkovich diamond indenter, calibrated on a fused silica standard sample with a Young's modulus of 72 GPa [41]. The tests were performed in a load control mode with a maximum load of 20 mN, loading/unloading rate of 40mN/min

and a grid spacing of 5 μm. The hardness and reduced elastic modulus were calculated according to the Oliver-Pharr method [41]. A Poisson's ratio of 0.22 was assumed for the HEC-Ni cermet [42].

3. Results and discussion

3.1 Thermodynamic simulations

The pseudo-binary phase diagram for the equimolar HEC-12 vol.% Ni cermet is presented in Fig. 1a. The dashed line indicates a total carbon content of 8.47 wt.%, as calculated from the starting powder composition. The compositionally complex system evolves to a simple two phase cubic structure of HEC-(Ti,V,Nb,Ta,W)C and nickel alloy binder. The HEC phase starts to become stable around 1300°C during solid state sintering. It slightly cuts through a phase region where graphite is also stable. To further clarify, one axis calculation was carried out at a fixed carbon content of 8.47 wt.% and the result in Fig. 1b showed an insignificant amount of graphite which disappears as the nickel starts to liquefy at 1324°C and only two phases i.e. carbide and binder are thermodynamically stable at higher temperatures. The chemical composition of the carbide and binder phases were also calculated as function of sintering temperature and are presented in Fig. 1 c and d, respectively. At lower temperature, the cubic carbides i.e. TiC, VC, NbC and TaC, which are known to be mutually soluble into each other [3], equally contribute to the FCC carbide phase formation. WC however continually dissolves into the carbide and binder phases as temperature increases. It has been reported that due to its lower vacancy formation energy, Ta tends to become a host to facilitate the interdiffusion among fellow metal-carbides during solid state sintering [16]. Based on the DFT (Density Functional Theory) calculations carried out by Yu et al. [43] the vacancy formation
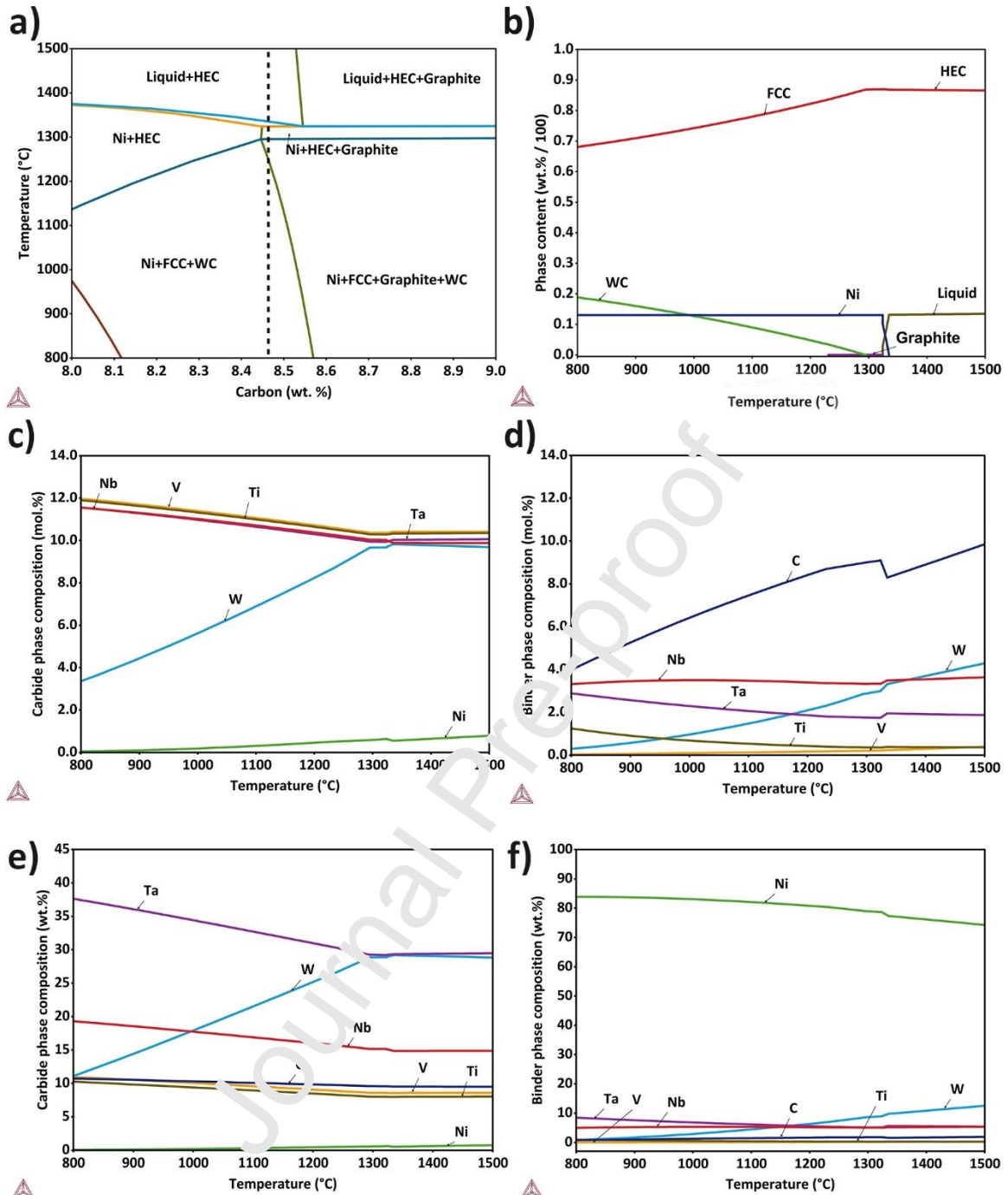
Figure 1. Calculated thermodynamic phase diagram for NbC-TiC-VC-WC-TaC-12 vol.% Ni (a) Mass fraction of all phases at 8.47 wt.% carbon content (b) Carbide phase content (c, e) and binder phase content (d, f) as function of sintering temperature.

energy (eV) of group IV and V elemental carbides in the ascending order are: TaC(3.5) < NbC(4.1) < VC(4.5) < TiC(8.6) < HfC(9.3) < ZrC(9.4). Therefore, it can be safely assumed that TaC together with NbC hosted the metal carbides for solid solution formation. The binder phase composition shows that NbC and TaC starts to diffuse into the nickel binder during the solid state sintering stage. However, the concentration of WC increases with temperature and eventually dominates the binder phase in the liquid phase sintering region as liquid nickel readily wets WC [44].

3.2 Thermal analysis

The DSC curve up to 1420°C is presented in Fig. 2, it is clear that the melting of nickel binder occurs in two steps, identified by two endothermic peaks at 1355°C and 1395°C respectively. Nickel forms the first eutectic with a solid solution of carbides formed during solid state sintering. The second eutectic is formed with pristine and/or a solid solution of TiC. During cooling however, the nickel binder solidifies with a single exothermic peak at 1370°C, suggesting a complete (Ti,V,Nb,Ta,W)C-HEC solid solution formation. The TGA curves are presented in Fig. 2 (b, c), the mass loss curve is discontinuous at 1355°C and follows a sharp descend at 1395°C. This significant mass loss is due to liquid nickel evaporation. Multiple peaks were identified on the mass loss rate curve (Fig. 2c). Peak 1, 2 and 3 could be associated with the carbothermal reduction of surface oxides present on the
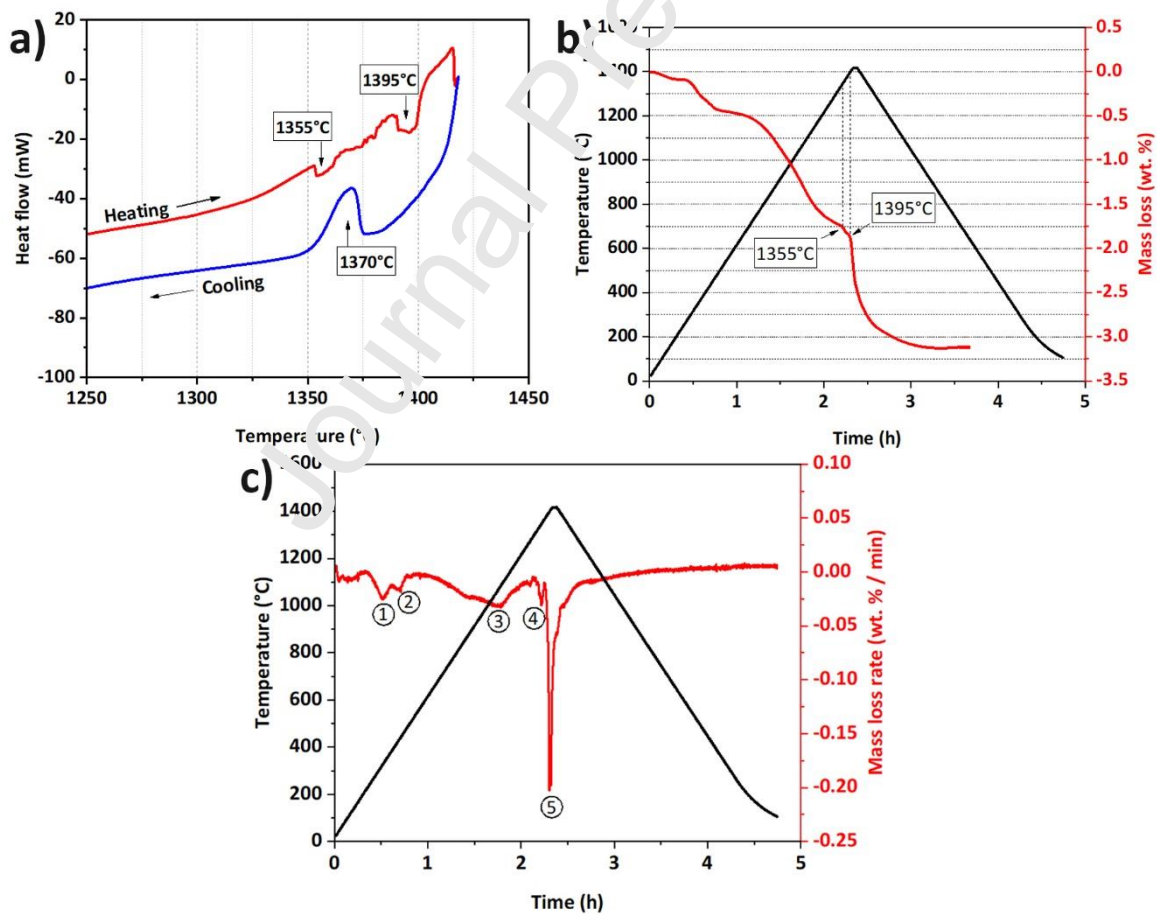

Figure 2. Thermal analysis for (Ti,V,Nb,Ta,W)C - 12 vol.% Ni at 1420°C for 10 min isothermal holding time, Differential Scanning Calorimetry (DSC) plot (a) and Thermogravimetric Analysis (TGA), mass loss curve (b) and mass loss rate curve (c).

starting powder mixture. The removal of these oxides is essential to allow wetting of the carbide phase by the binder. Three carbothermal reduction peaks have been reported for cemented carbides, accompanied by CO_2 (250-500°C) and CO (500-1000°C) formation [45,46]. Peaks 4 and 5 are rather sharp and correspond to the two eutectic temperatures. L. Chen *et al.* [47,48] identified the eutectic temperatures of cermets containing NbC, TaC, WC, TiC, TiN, (Ti,W)(C,N) and Co/Ni to be between 1350°C and 1400°C. Moreover, a careful examination of the pseudobinary phase diagram (Fig 1a) also revealed that, at nominal equimolar carbide composition, the nickel binder traverses through a small liquid + Ni + HEC phase region before approaching the Liquid + HEC liquidus line, which is also in good agreement with the thermal analysis.

3.3   Microstructure and phase analysis

The elemental distribution of the top surface of a green powder compact is presented in Fig. 3, showing that the starting powders are well distributed with an average particle size ≤ 2 µm. The ductile nickel particles were elongated during the wet milling process. Optical and BSE scanning electron micrographs of solid state and liquid phase sintered HEC-cermets are presented in Fig. 4 and Fig. 5, respectively. The relative density, grain size, contiguity, carbon analysis and apparent porosity are compared in Table 2. The microstructure of the cermet sintered at 1300°C is highly porous. The grain size and contiguity of the cermet sintered at 1300°C could not be determined because of its indiscernible grain boundaries. However, the microstructure represented a solid-state sintered cermet with interconnected porosity and undissolved WC and TiC particles with bright and dark atomic number contrasts respectively, as verified by the compositional analysis in Fig. 6a. At 1360°C, a 94% densified cermet was obtained with isolated porosity and no remnant WC phase, indicating the onset of liquid phase formation as indicated in the DSC-TGA (Fig. 2).
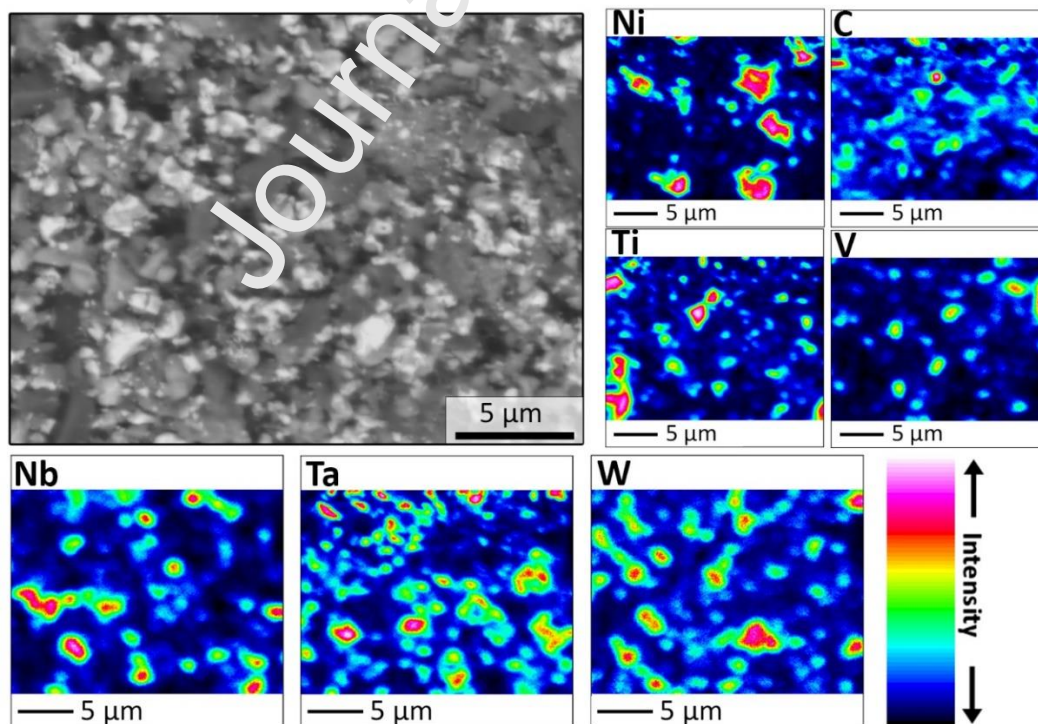

Figure 3. EPMA elemental mapping of the top surface of a green powder compact.

Table 2. Sintered density, relative density, grain size, contiguity, porosity and carbon to metal mole ratio for (Ti,V,Nb,Ta,W)C-12 vol.% Ni cermets at different sintering temperatures.

Sintering Temperature (°C)	Sintered density (g/cm³)	Relative density (%)	Carbide grain size (µm)	Contiguity	Apparent porosity (ISO-4505)	C/(Ti,V,Nb,Ta,W) Coulometry
1300	7.21	73.6	/	/	A08B04C00	
1360	9.19	93.8	1.13 ± 0.07	0.89 ± 0.03	A06B00C00	/
1390	9.83	100.3	0.93 ± 0.11	0.85 ± 0.05	A02B00C00	
1420	9.87	100.7	1.80 ± 0.26	0.80 ± 0.06	A00B00C00	0.86 ± 0.02

The cermet sintered at 1390°C was fully densified with a two-phase microstructure and almost no apparent porosity. This verifies that the cermet was in the liquid phase sintering region. The nickel binder distribution however, remained moderate with increasing temperature and a connected carbide phase microstructure with high contiguity was realized which shows a modest wettability of HEC phase and nickel binder. A smaller grain size was observed at 1390°C when liquid binder starts to impregnate the skeletal carbide structure. The microstructure however (Fig. 4c) showed some partially dissolved TiC in the
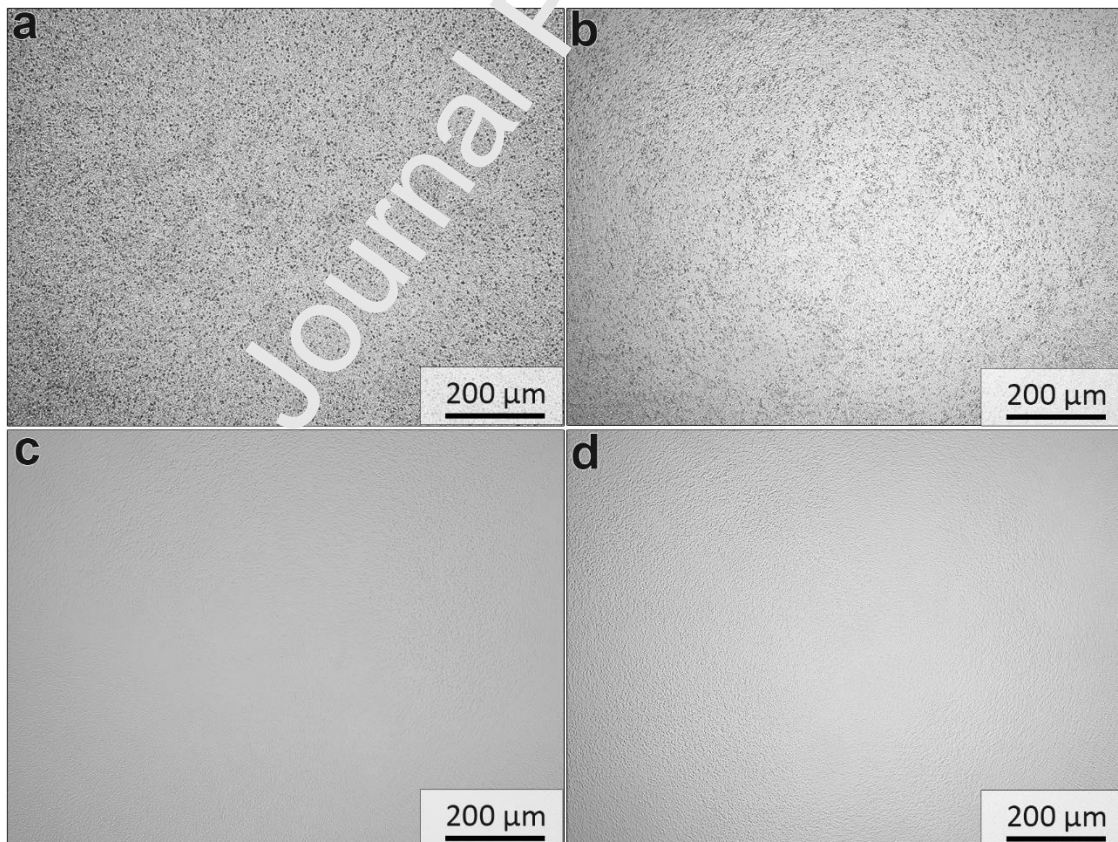

Figure 4 Light Optical Microscopy (LOM) at 100x magnification of the (Ti,V,Nb,Ta,W)C-12 vol.% Ni cermets sintered at 1300°C (a), 1360°C (b), 1390°C (c) and 1420°C (d).

core and at carbide/binder interfaces. A closer look, shown in the magnified inset in Fig. 5 c, reveals that a dark atomic contrast phase is also present at the grain boundary interfaces of some carbides (indicated with arrows). This dark phase is remnant TiC from the starting powder mixture.
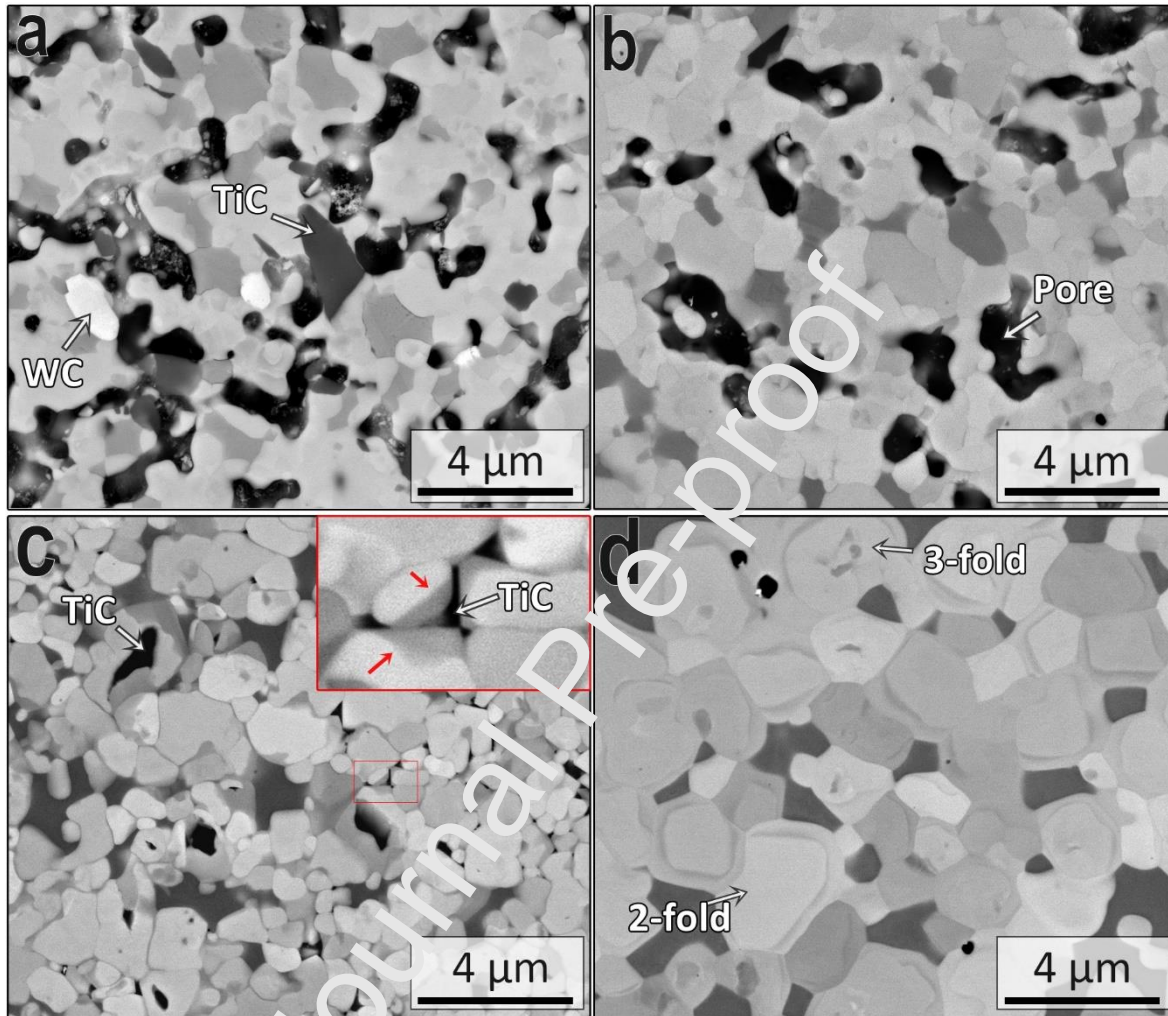

Figure 5. BSE micrographs NbC-TiC-VC-WC-TaC-12 vol.% Ni sintered for 90 min at 1300°C (a), 1360°C (b), 1390°C (C) and 1420°C (d).

Wavelength dispersive elemental mappings of the HEC cermet sintered at 1390°C are given in Fig. 6 b. This remnant phase could be attributed to the delayed solubility of TiC in the nickel binder amid the saturation by highly soluble WC and VC constituents. Moreover, The solubilities (wt.%) of carbides in a nickel binder at 1400°C were determined by P. Ettmayer *et. al.* [49] WC (27) < VC (14) < TiC (11) < NbC (7.0) < TaC (6.3). Therefore, the cermet was sintered at a higher sintering temperature of 1420°C and a fully dense two-phase microstructure without porosity and/or remnant TiC was obtained (Fig. 4 d and 5 d). The black spots within the carbide phase are most likely residual oxides from the starting powder mixture. The WDS elemental mapping and line scan are presented in Fig. 6 (c, d). It is clear that the dark atomic contrast phase in the BSE micrograph represents the nickel binder, which is present in an isolated manner within the contiguous light atomic number contrast HEC phase. The concentration of transition metals and carbon is dominant in the carbide phase. However, a careful examination revealed that the BSE micrograph contains

two types of core-rim structured carbide grains with 2-fold and 3-fold structures. The 2-fold carbide grains consist of a bright core, dark inner rim and a bright outer rim whereas 3-fold carbide grains consist of a dark core, bright inner rim, dark intermediate rim and a bright outer rim. This contrast can be correlated with elemental mapping results revealing that the bright contrast is due to a higher concentration of heavy elements i.e. Ta and W, the dark core is due to the higher concentration of intermediate elements i.e. Nb and V whereas the dark inner rim is due to the light atomic weight Ti. In light of the foregoing discussion, Nb and Ta formed a host for fellow metal carbides to form cubic HEC grains with Nb-rich dark core (2-fold) and Ta-rich bright core (3-fold) structured grains. The delayed the dissolution of TiC resulted in the formation of a fine dark inner rim in both types of carbide grains whereas the bright outer rim is caused by solution re-precipitation. The W elemental map clearly shows, the remains of W

in the binder region, as indicated by the light blue concentration shade in Fig. 6 a. This
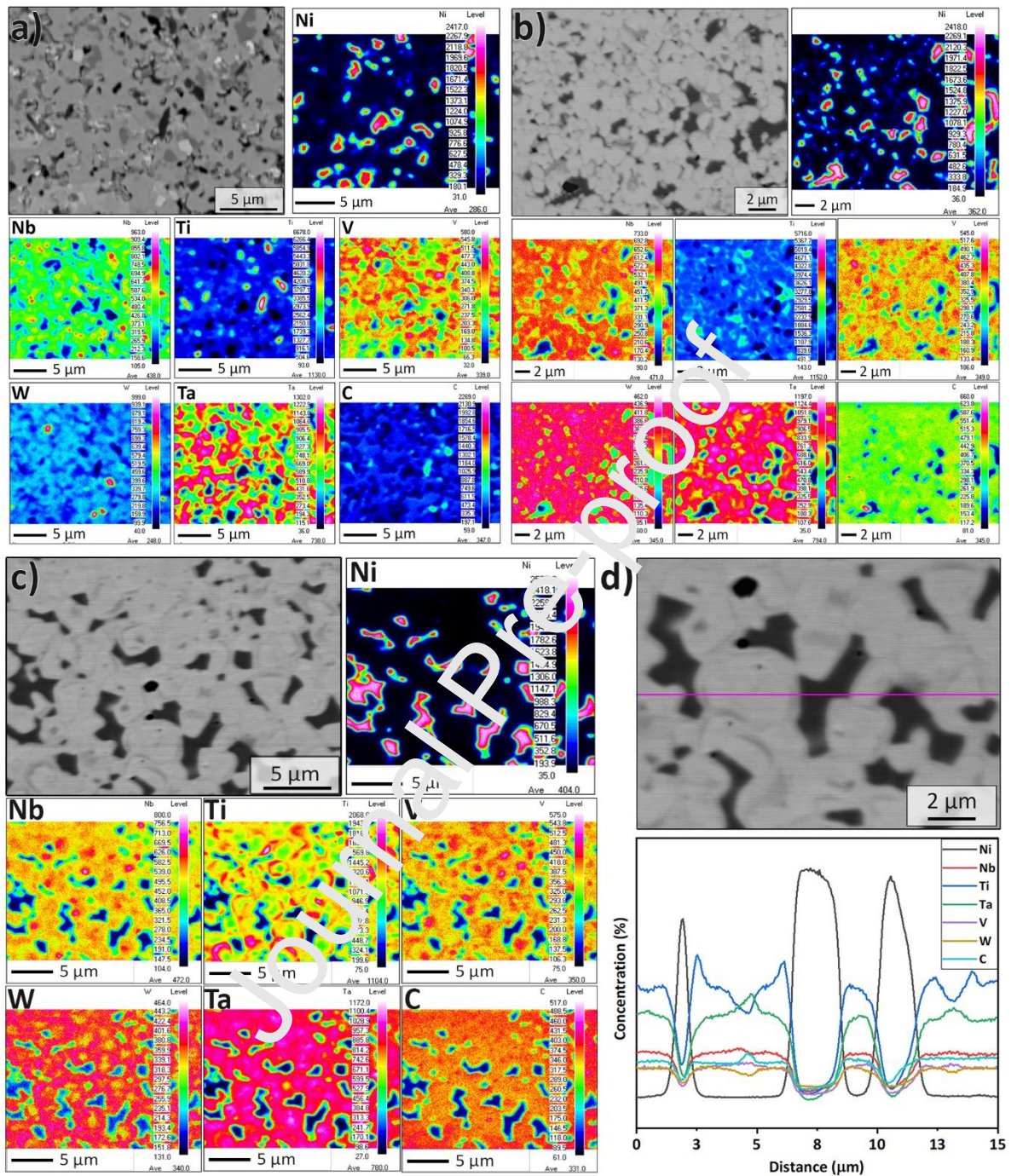

Figure 6. WDS elemental mapping of (Ti,V,Nb,Ta,W)C-12 vol.% Ni cermets sintered at 1300°C (a), 1390°C (b) and 1420°C (c) and a Line scan of cermet sintered at 1420°C (d).

distribution of elements across the carbide grains is further elaborated by the line scan. The concentration of Ti and W in the rim is clearly distinguishable from that of the core, which is higher in Ta, Nb, V and C concentration.

Spot	Ti (Kα)	V (Kα)	Nb (Lα)	Ta (Mα)	W (Lα)	Ni (Kα)
1	10.12	11.30	12.81	12.51	9.56	0.72
2	10.54	11.61	14.92	9.69	9.25	0.85
3	10.93	10.89	12.57	11.89	9.71	0.78
4	11.93	10.08	11.88	11.22	10.54	0.79
5	12.48	9.91	11.50	10.78	10.68	1.22
6	11.17	10.47	12.05	11.66	10.01	0.67
7	11.58	10.43	13.31	10.50	9.97	1.04
8	11.08	11.45	13.98	10.13	8.86	0.82
9	3.35	4.23	3.12	3.20	6.17	67.17

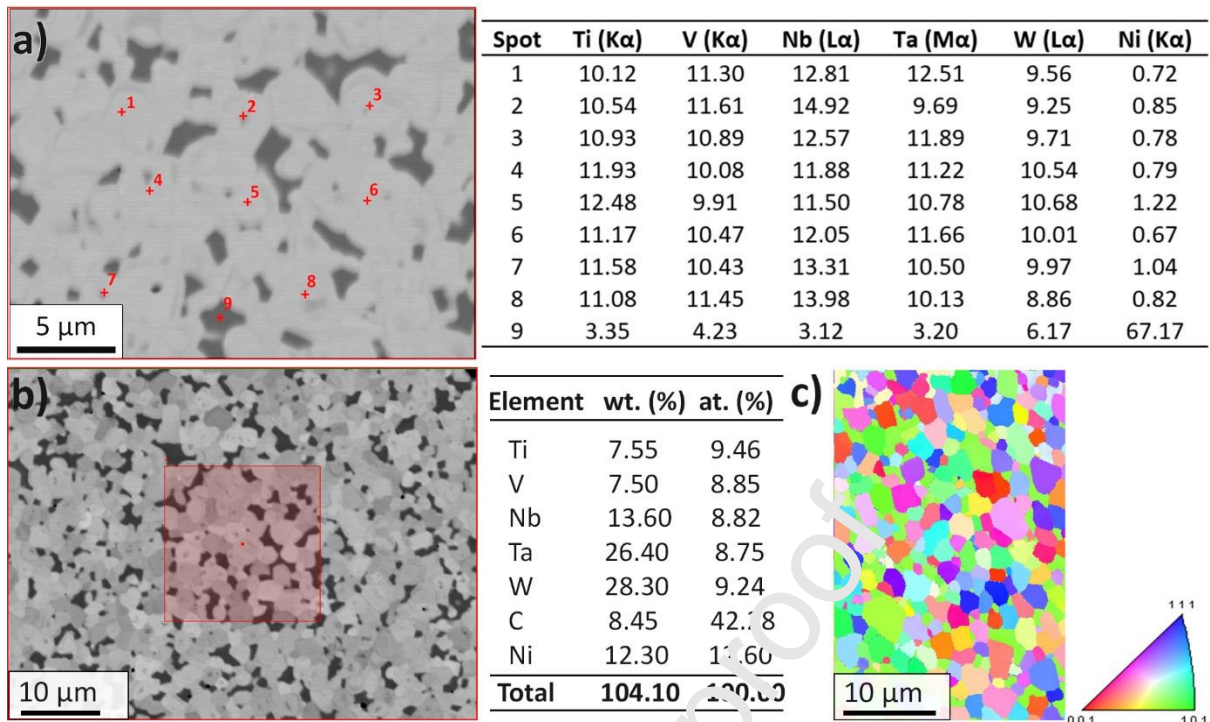| Element	wt. (%)	at. (%)
Ti	7.55	9.46
V	7.50	8.85
Nb	13.60	8.82
Ta	26.40	8.75
W	28.30	9.24
C	8.45	42.?8
Ni	12.30	1?.60
Total	104.10	??0.?0

Figure 7. EPMA for (Ti,V,Nb,Ta,W)C-12 vol.% Ni sintered at 1420°C for 90 min spot analysis (at.%) (a) area analysis (b) and a representative Inverse Pole Figure (IPF) map (c).

In order to verify the homogeneity of the HEC phase, EPMA point analysis were carried out on eight randomly selected HEC grains and the binder phase, as presented in Fig. 7a. The chemical composition of different grains showed similar values, implying that the microstructure is homogeneous. It is well known that carbides of transition metals can be considerably sub-stoichiometric [3]. Therefore, the degree of sub-stoichiometry in the two-phase sintered cermets was estimated for the (Ti,V,Nb,Ta,W)C-12 vol.% Ni sintered at 1420°C from carbon combustion analysis to be 0.86 (Table 2). The thermodynamically calculated carbon stoichiometry in fcc-HEC phase as function of temperature is presented in Fig. 8a, revealing a decreasing trend from the solid state sintering towards the liquid phase sintering region. The measured carbon to metal ratio in the sintered cermet was considerably lower as compared to the thermodynamically calculated value (0.97 at 1420°C) due to two plausible reasons, i.e. carbon loss due to carbothermal reduction of oxides and technical constraints in accurate carbon content analysis. For comparison, T.J. Harrington *et al.* [25] reported a sub-stoichiometry of 0.85 for an equimolar (Ti,V,Nb,Ta,W)C HEC, sintered at 2200°C under a carbon rich environment, implying an equilibrium sub-stoichiometric carbon content for the HEC composition. EPMA area analysis and an Inverse Pole Figure (IPF) map of a representative HEC cermet are shown in Fig. 7 (b and c). The quantitative analysis holds good conformity with the nominal material composition which confirms that the cermet is a nickel bonded HEC, with 5-35 at.% of five different transition metals as defined by Yeh *et al* [29]. The IPF map reveals that the cermet is composed of randomly distributed crystals with no preferred orientation.

The evolution of the thermodynamic properties of the HEC-Ni system, as function of temperature is shown in Fig. 8b, indicating a decreasing Gibbs free energy and an increasing entropy and enthalpy with the increasing temperature. This implies that at higher temperatures or prolonged holding times at liquid phase sintering temperatures, the system

will continue to prevail the two-phase fcc structure and the HEC grains will continue to grow by Ostwald ripening to achieve the lowest possible Gibbs free energy by reducing the number of grain boundaries.
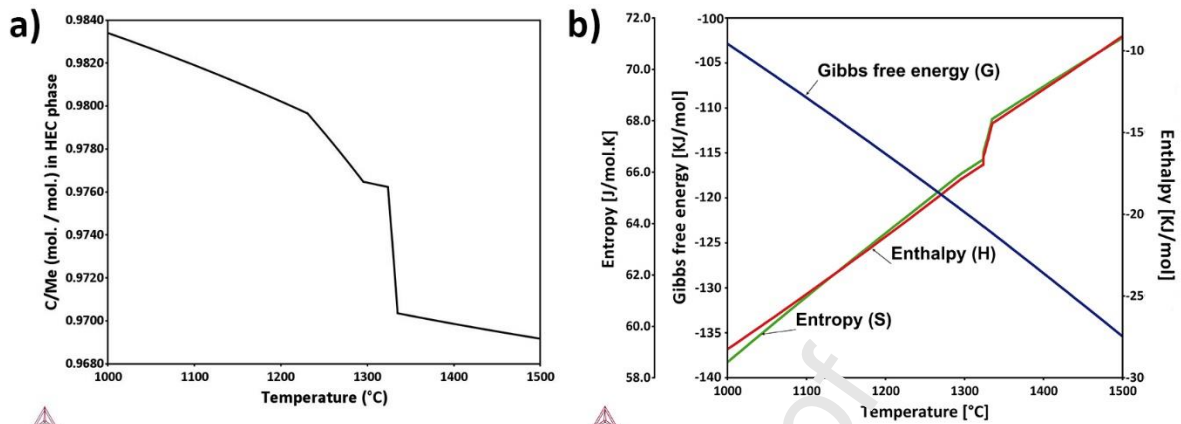

Figure 8. Calculated carbon content in HEC phase (a) and thermodynamic properties (b) for the (Ti,V,Nb,Ta,W)C - 12 vol.% Ni cermet system as function of temperature.

3.4 Phase analysis and lattice parameter

In order to examine the phase evolution as function of temperature, X-ray diffraction patterns of the HEC-cermets were acquired, as shown in Fig. 9 (a-c). The XRD pattern of the starting power reveals the characteristic peaks of the monocarbides and nickel. No significant change was observed at 900 and 1000°C. At 1200°C, the high intensity TaC/NbC peaks started to shift towards higher 2θ values, implying a shrinkage of the cubic lattice parameter. The individual peaks of VC and TiC disappeared and the diffraction pattern only contained peaks of WC, a FCC solid solution carbide and nickel. At 1300°C, the characteristic peaks of TaC/NbC completely disappeared whereas WC peaks remained, which is consistent with the thermodynamic simulations (Fig. 1 a, b) and microscopy analysis (Fig. 5 a). At 1360 - 1420°C, the XRD pattern evolves to a simple two-phase fcc carbide and fcc nickel alloy binder phase. The evolution of the XRD patterns indicates that HEC solid solution formation initiated at 1200°C and was completed at 1360°C. The remnant TiC phase, observed in the BSE micrographs at 1360 and 1390°C (Fig. 5 b, c), could not be detected in the XRD pattern. However, as discussed earlier a complete solid solution was only realized during liquid phase sintering of 1420°C with the formation of (Ti,V,Nb,Ta,W)C with a lattice parameter of 4.3601 Å, consistent with published literature values [50]. The lattice parameter of the nickel binder increased continuously up to 1300°C due to the dissolution of metal atoms from the dissolving carbides. The atomic radius (pm) of the constituent elements are: Nb (146), Ti (147), V (134), W (139), Ta (146), Ni (124) [3]. The lattice parameter of the Ni binder however drops above 1300°C, probably due to the replacement of Ta and Nb by smaller W, as indicated by the thermodynamic calculations (Fig. 1 d). The elemental mapping of the HEC cermet sintered at 1390°C (Fig. 6 b) showed a relatively higher W concentration in the binder phase as compared to Fig. 6c. The cermet sintered at 1420°C showed grain growth and the lower solute content resulted in a decreased lattice parameter of the nickel binder phase.
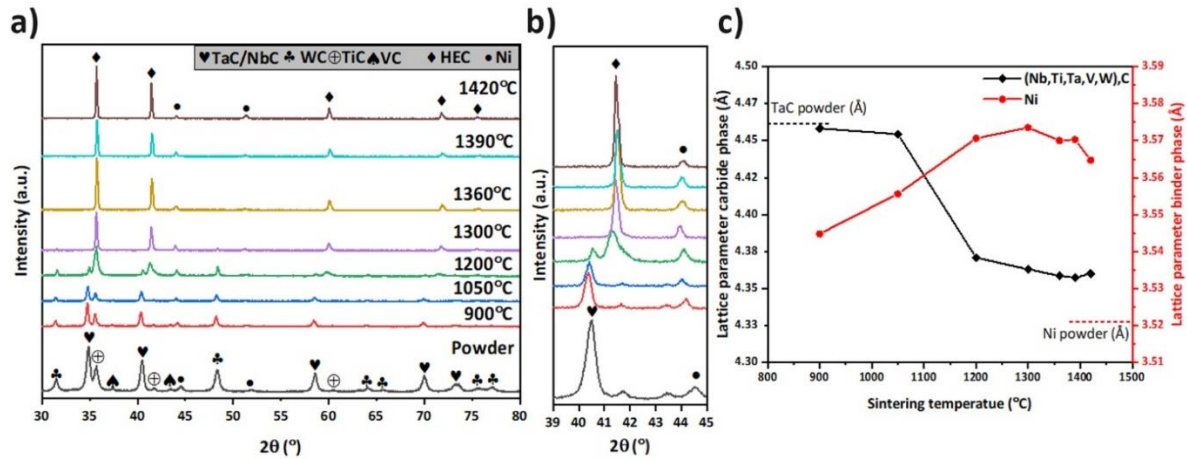
Figure 9. XRD patterns of the HEC-Ni cermet starting powder mixture as function of temperature, demonstrating the evolution of the monocarbides and nickel powder mixture into a two phase cubic (Nb,Ti,V,W,Ta)C high entropy carbide and nickel alloy binder phase (a), magnified peaks for carbide and binder phases (b) and influence of sintering temperature on the lattice parameter of carbide and binder phases (c).

Table 3. Nanoindentation hardness and stiffness, Vickers hardness and Palmqvist toughness of liquid phase sintered HEC-Ni cermets.

Material	Sintering temperature	H (GPa)	E (GPa)	HV (GPa)	K_{1C} (MPa.m$^{1/2}$)
(Ti,V,Nb,Ta,W)C-12 vol.% Ni	1420°C	23.0 ± 6.0	358 ± 35	14.26 ± 0.4	9.2 ± 0.2
(Ti,V,Nb,Ta,W)C-12 vol.% Ni	1390°C	/	/	14.45 ± 0.6	9.5 ± 0.5
(Ti,V,Nb,Ta,W)C [25]	2200°C	28 ± 2	485 ± 36	/	/
(Ti,V,Nb,Ta,W)C-19.2 vol.% Co [31]	1400°C	/	/	14.32 ± 0.1	6.7 ± 0.2

3.5 Mechanical properties

The mechanical properties of the liquid phase sintered (Ti,V,Nb,Ta,W)C-Ni cermets are presented in Table 3. The nanoindentation hardness and elastic modulus are compared with those of a spark plasma sintered binderless (Ti,V,Nb,Ta,W)C high entropy carbide [25], whereas the microhardness and Palmqvist toughness are compared with a gas pressure sintered (Sinter-HIP) (Ti,V,Nb,Ta,W)C-19.2 vol.% Co [31]. The liquid phase sintered (Ti,V,Nb,Ta,W)C-Ni cermets were fully densified. Despite the bigger grain size and lower contiguity (Table 2), the cermet sintered at 1420°C had a lower hardness and comparable fracture toughness (14.26 ± 0.4 GPa and 9.2 ± 0.2 MPa.m$^{1/2}$) as compared to the cermet sintered at 1390°C (14.45 ± 0.6 GPa and 9.5 ± 0.5 MPa.m$^{1/2}$). The slightly lower mechanical properties of the former could be attributed to the formation of core-rim interfaces which could act as sites for of crack initiation [51]. At 1420°C, the TiC completely dissolved and precipitated in the rim area of the HEC phase increasing the hardness of the carbide phase by solid solution strengthening but the fracture toughness decreased. The nanoindentation hardness and elastic modulus of the HEC-cermet are evidently lower than for a reference
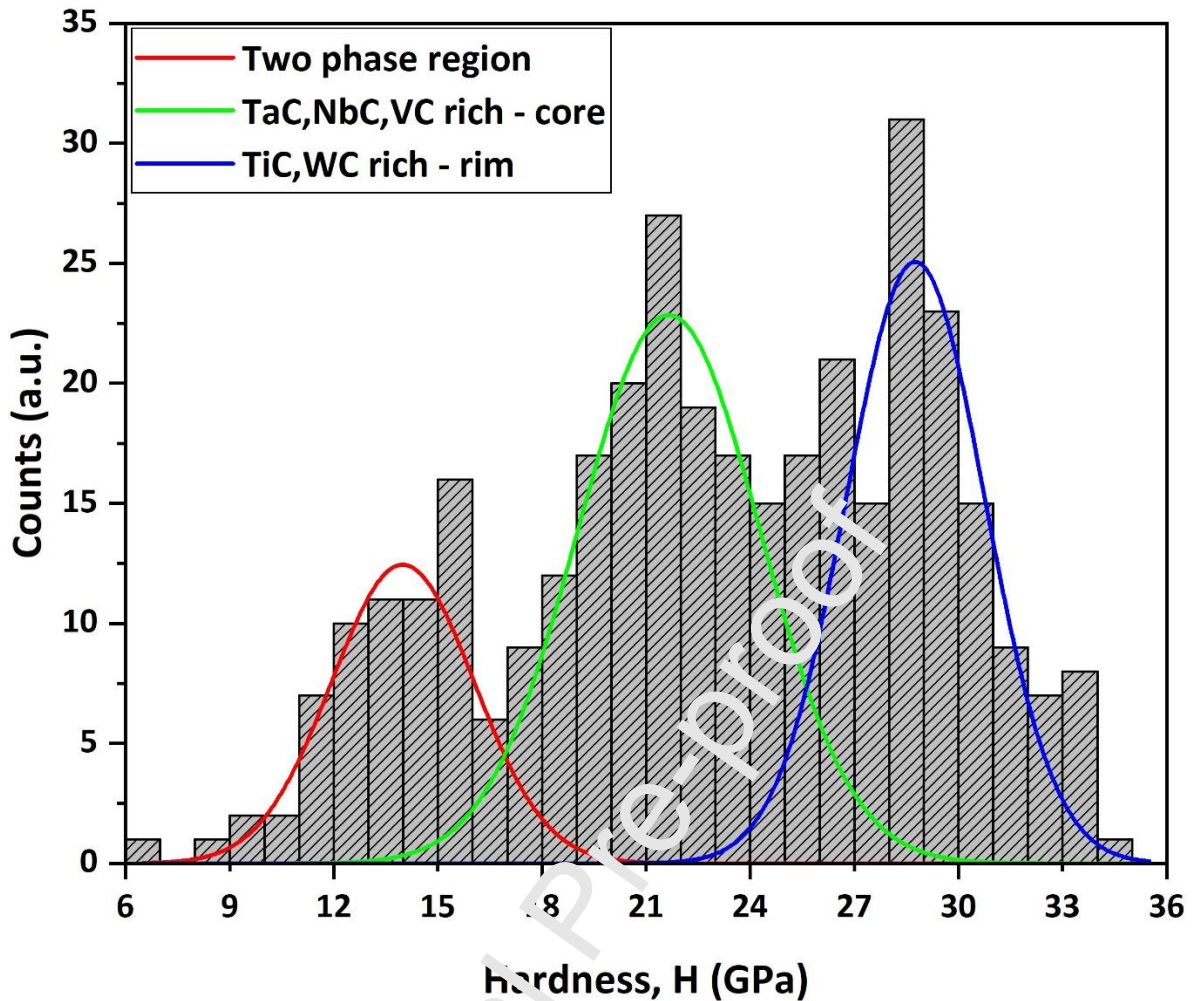
Figure 10. Deconvoluted hardness values (bin size 1 GPa) of 350 nanoindentations performed in a load control mode to a maximum load of 20 mN.

binderless (Ti,V,Nb,Ta,W)C ceramic, due to the presence of the ductile nickel binder. Moreover, the standard deviation on the nano-hardness measurements is quite high in the HEC-cermet and the deconvoluted nano-hardness distribution shown in Fig. 10 reveals a tri-modal distribution corresponding to the carbide/binder interfaces, (Ta,Nb,V)C rich carbide cores and (Ti,W)C rich rim areas, respectively. These results clearly show a substantial hardness difference between the carbide grain core (22 ± 0.3 GPa) and rim (29 ± 0.3 GPa), which can be correlated with the composition analysis in Fig. 6 (a, b). The reported nano hardness (max. load 300 mN) of transition metal carbides in descending order is: TiC (31 GPa) > VC (29 GPa) > WC (27 GPa) > NbC (17 GPa) > TaC (14 GPa) [25], indicating a potential hardening effect of Ti and W versus Ta and Nb. A representative nanoindentation grid map along with its electron backscattering diffraction (EBSD) Inverse Pole Figure map (IPF) and a randomly selected nanoindentation in the rim area are shown in Fig. 11. The majority of the nanoindentations were without crack formation, which shows that TaC and NbC not only hosted the metal carbides but also carried along their inherent ductile characteristics, as indicated by the slip lines [52]. Moreover, the load-displacement curves are smooth without structure, pop-in events. Representative crack propagation patterns and fractured surfaces for (Ti,V,Nb,Ta,W)C-Ni cermets sintered at 1390°C and 1420°C are presented in Fig. 12 (a-d). In general, the cracks followed a mixed trans and intergranular trajectory through the

composite structure, revealing active toughening mechanisms like crack deflection and crack
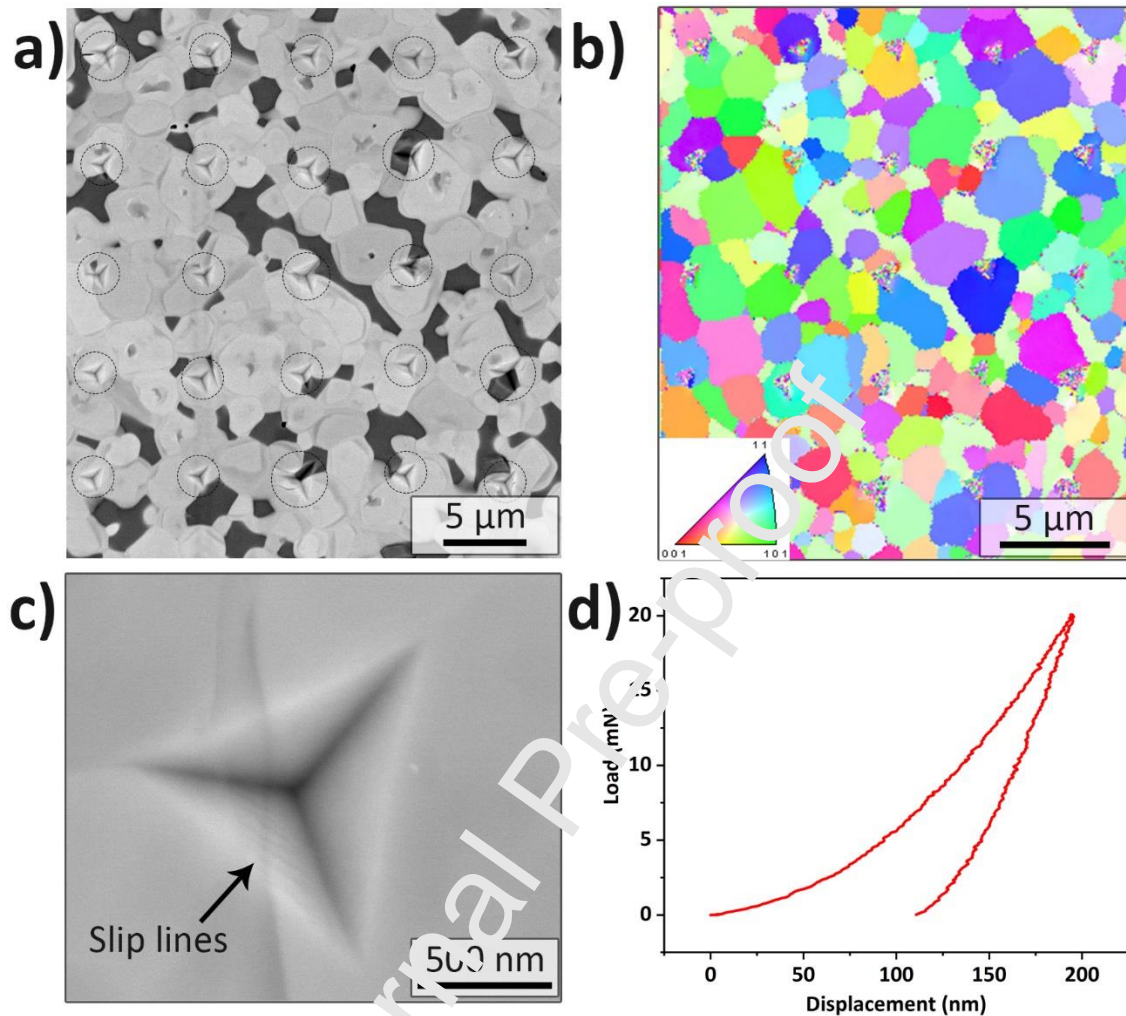

Figure 11. Representative nanoindentation grip map (a), IPF map of the grid map (b), a randomly selected nanoindent at the run area of HEC phase (c), and load-displacement curve for the nanoindent (d).

bridging. The higher fracture toughness of the cermet sintered at 1390°C could be correlated with the dominant intergranular fracture pattern and solid solution strengthening of the nickel binder with higher remnant solute content (Fig. 6 d). Despite the grain growth and reduced river-like patterns which indicate a higher fracture toughness of cleaved carbide grains [53]. Carbide grains with remnant plastically deformed binder phase (characteristic of intergranular fracture) are more dominant in the cermet sintered at 1390°C. The nickel binder in both cermets showed ductile dimple (red arrows) features.

4. Conclusions

A high entropy carbide cermet based on TiC, VC, NbC, TaC, and WC monocarbides as well as 12 vol.% Ni was prepared using conventional liquid phase sintering. The microstructure and phase analysis carried out in the solid state and liquid sintering regimes correlated well with the thermodynamic simulations. The solid state sintered cermets showed a lower relative density and remnant starting powder components, whereas full

densification was achieved upon liquid phase sintering above 1360°C. A single cubic (Ti,V,Nb,Ta,W)C phase carbide with a (Ta,Nb,V)-rich core and a (Ti,W)-rich rim structure was obtained when sintered at 1420°C. XRD and SEM phase analysis showed a progressive dissolution of the multi-component powder mixture into FCC (Ti,V,Nb,Ta,W)C-high entropy carbide and nickel alloy binder phases. TaC and NbC were identified as host phases for solid solution carbide phase formation, whereas WC and TiC only completely dissolved above 1300°C and 1360°C, respectively. The delayed dissolution of TiC was reflected in a locally Ti-enriched carbide rim structure, with dark atomic number contrast and enhanced hardness. The solid state sintered cermets showed a lower relative density and remnant starting powder components, whereas full densification was achieved upon liquid phase sintering above 1360°C. A single cubic (Ti,V,Nb,Ta,W)C phase carbide with a (Ta,Nb,V)-rich core and a (Ti,W)-rich rim structure was obtained when sintered at 1420°C. Nanoindentation analysis revealed a much harder rim (29 ± 0.3 GPa) structure surrounding a lower hardness core (22 ± 0.3 GPa). The TaC and NbC hosted cubic solid solution lattice showed high plasticity during nanoindentation, which rendered a contiguous structured cermet with an acceptable fracture toughness for wear resistant applications.
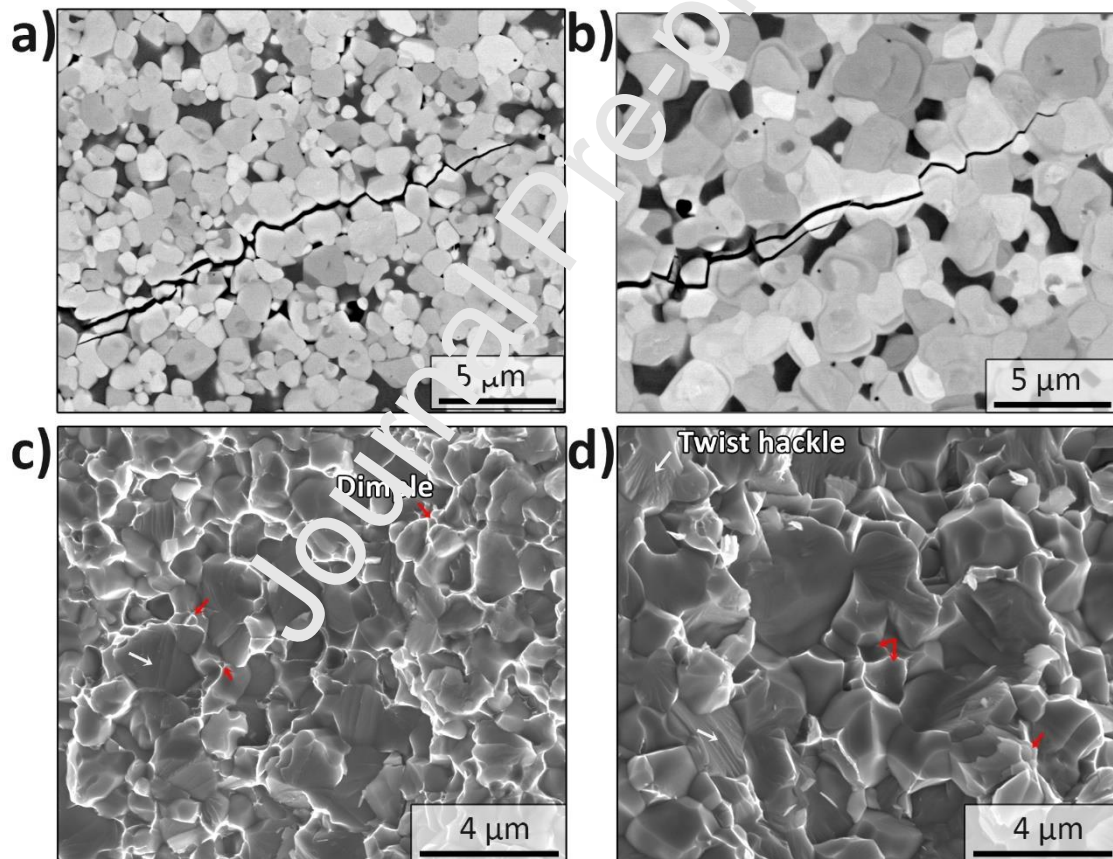

Figure 12. SEM micrographs of the crack propagation path originating from an indentation corner and fractured surface of the HEC cermet sintered at 1390°C (a, c) and 1420°C (b, d).

CRediT author statement

Zahid Anwer: Investigation, Validation, Software, Formal analysis, Visualization, Data curation and Writing – original draft. **Shuigen Huang**: Conceptualization, Methodology,

Supervision, Funding acquisition and Writing – review & editing. **Jozef Vleugels**: Supervision, Resources and Writing – review & editing.

Declaration of competing interest

The authors declare that they have no known competing financial interests or personal relationships that could have appeared to influence the work reported in this paper.

Acknowledgement

References

[1] E. Wuchina, E. Opila, M. Opeka, W. Fahrenholtz, I. Talmy, UHTCs: Ultra-High Temperature Ceramic materials for extreme environment applications, Electrochem. Soc. Interface. 16 (2007) 30–36. https://doi.org/10.1149/2.f04074if.

[2] A.S. Kurlov, A.I. Gusev, Tungsten Carbides: Structure, Properties and Application in Hardmetals, 2013. https://doi.org/10.1007/978-3-319-00524-9.

[3] H.O. 0 Pierson, Handbook of refractory carbides and nitrides : properties, characteristics, processing, and applications, Noyes Publications westwood, New Jersey, U.S.A, 1996.

[4] V.K. Sarin, Comprehensive Hard Materials Vol. 1, Elsevier, 2014.

[5] H.E. Exner, Physical and chemical nature of cemented carbides, Int. Met. Rev. 24 (1979) 149–173. https://doi.org/10.1179/imtr.1979.24.1.149.

[6] J. García, V. Collado Ciprés, A. Blomqvist, B. Kaplan V.C. Ciprés, A. Blomqvist, B. Kaplan, Cemented carbide microstructures: a review, Int. J. Refract. Met. Hard Mater. 80 (2019) 40–68. https://doi.org/10.1016/j.ijrmhm.2018.12.004.

[7] A.H. Tkaczyk, A. Bartl, A. Amato, V. Lapkovskis, M. Petranikova, Sustainability evaluation of essential critical raw materials: cobalt, niobium, tungsten and rare earth elements, J. Phys. D. Appl. Phys. 51 (2018) 203001. https://doi.org/10.1088/1361-6463/AABA99.

[8] R. Lauwerys, D. Lison, Health risks associated with cobalt exposure — an overview, Sci. Total Environ. 150 (1994) 1–6. https://doi.org/10.1016/0048-9697(94)90125-2.

[9] J.M. Torralba, P. Alvaredo, A. García-Junceda, High-entropy alloys fabricated via powder metallurgy. A critical review, Powder Metall. 62 (2019) 84–114. https://doi.org/10.1080/00325899.2019.1584454.

[10] M. Woydt, H. Mohrbacher, J. Vleugels, S. Huang, Niobium carbide for wear protection – tailoring its properties by processing and stoichiometry, Met. Powder Rep. 71 (2016) 265–272. https://doi.org/10.1016/j.mprp.2015.12.010.

[11] Y. Peng, H. Miao, Z. Peng, Development of TiCN-based cermets: Mechanical properties and wear mechanism, Int. J. Refract. Met. Hard Mater. 39 (2013) 78–89. https://doi.org/10.1016/j.ijrmhm.2012.07.001.

[12] C.S. Chen, C.C. Yang, H.Y. Chai, J.W. Yeh, J.L.H. Chau, Novel cermet material of WC/multi-element alloy, Int. J. Refract. Met. Hard Mater. 43 (2014) 200–204. https://doi.org/10.1016/j.ijrmhm.2013.11.005.

[13] E. Holmström, R. Lizárraga, D. Linder, A. Salmasi, W. Wang, B. Kaplan, H. Mao, H. Larsson, L. Vitos, High entropy alloys: Substituting for cobalt in cutting edge technology, Appl. Mater. Today. 12 (2018) 322–329. https://doi.org/10.1016/j.apmt.2018.07.001.

[14] C.M. Rost, E. Sachet, T. Borman, A. Moballegh, E.C. Dickey, D. Hou, J.L. Jones, S. Curtarolo, J.-P. Maria, Entropy-stabilized oxides, Nat. Commun. 2015 61. 6 (2015) 1–

8. https://doi.org/10.1038/ncomms9485.

[15]   J. Gild, Y. Zhang, T. Harrington, S. Jiang, T. Hu, M.C. Quinn, W.M. Mellor, N. Zhou, K. Vecchio, J. Luo, High-Entropy Metal Diborides: A New Class of High-Entropy Materials and a New Type of Ultrahigh Temperature Ceramics, Sci. Reports 2016 61. 6 (2016) 1–10. https://doi.org/10.1038/srep37946.

[16]   E. Castle, T. Csanádi, S. Grasso, J. Dusza, M. Reece, Processing and Properties of High-Entropy Ultra-High Temperature Carbides, Sci. Reports 2018 81. 8 (2018) 1–12. https://doi.org/10.1038/s41598-018-26827-1.

[17]   X. Yan, L. Constantin, Y. Lu, J.F. Silvain, M. Nastasi, B. Cui, (Hf0.2Zr0.2Ta0.2Nb0.2Ti0.2)C high-entropy ceramics with low thermal conductivity, J. Am. Ceram. Soc. 101 (2018) 4486–4491. https://doi.org/10.1111/jace.15779.

[18]   P. Sarker, T. Harrington, C. Toher, C. Oses, M. Samiee, J.-P.P. Maria, D.W. Brenner, K.S. Vecchio, S. Curtarolo, High-entropy high-hardness metal carbides discovered by entropy descriptors, Nat. Commun. 2018 91. 9 (2018) 1–10. https://doi.org/10.1038/s41467-018-07160-7.

[19]   J. Dusza, P. Švec, V. Girman, R. Sedlák, E.G. Castle, T. Csanádi, A. Kovalčíková, M.J. Reece, Microstructure of (Hf-Ta-Zr-Nb)C high-entropy carbide at micro and nano/atomic level, J. Eur. Ceram. Soc. 38 (2018) 4303–4307. https://doi.org/10.1016/J.JEURCERAMSOC.2018.05.006.

[20]   M. Qin, J. Gild, C. Hu, H. Wang, M.S. Bin Hoque, J.L. Braun, T.J. Harrington, P.E. Hopkins, K.S. Vecchio, J. Luo, Dual-phase high-entropy ultra-high temperature ceramics, J. Eur. Ceram. Soc. 40 (2020) 5037–5050. https://doi.org/10.1016/j.jeurceramsoc.2020.05.040.

[21]   Y. Yang, L. Ma, G.Y. Gan, W. Wang, B.Y. Tang, Investigation of thermodynamic properties of high entropy (TaNbHfTiZr)C and (TaNbHfTiZr)N, J. Alloys Compd. 788 (2019) 1076–1083. https://doi.org/10.1016/j.jallcom.2019.02.254.

[22]   O.F. Dippo, N. Mesgarzadeh, T.J. Harrington, G.D. Schrader, K.S. Vecchio, Bulk high-entropy nitrides and carbonitrides, Sci. Rep. 10 (2020) 1–11. https://doi.org/10.1038/s41598-020-78175-8.

[23]   J. Gild, J. Braun, K. Kaufmann, E. Marin, T. Harrington, P. Hopkins, K. Vecchio, J. Luo, A high-entropy silicide: (Mo0.2Nb0.2Ta0.2Ti0.2W0.2)Si2, J. Mater. 5 (2019) 337–343. https://doi.org/10.1016/j.jmat.2019.03.002.

[24]   X. Chen, Y. Wu, High-entropy transparent fluoride laser ceramics, J. Am. Ceram. Soc. 103 (2020) 750–756. https://doi.org/10.1111/jace.16842.

[25]   T.J. Harrington, J. Gild, P. Sarker, C. Toher, C.M. Rost, O.F. Dippo, C. McElfresh, K. Kaufmann, E. Marin, L. Borowski, P.E. Hopkins, J. Luo, S. Curtarolo, D.W. Brenner, K.S. Vecchio, Phase stability and mechanical properties of novel high entropy transition metal carbides, Acta Mater. 166 (2019) 271–280. https://doi.org/10.1016/j.actamat.2018.12.054.

[26]   Y. Wang, Processing and properties of high entropy carbides, Adv. Appl. Ceram. 0 (2021) 1–22. https://doi.org/10.1080/17436753.2021.2014277.

[27] D. Ni, Y. Cheng, J. Zhang, J. Liu, Advances in ultra-high temperature ceramics , composites , and coatings, 11 (2022) 1–56.

[28] D.B. Miracle, High entropy alloys as a bold step forward in alloy development, Nat. Commun. 10 (2019) 1–3. https://doi.org/10.1038/s41467-019-09700-1.

[29] J.W. Yeh, S.K. Chen, S.J. Lin, J.Y. Gan, T.S. Chin, T.T. Shun, C.H. Tsau, S.Y. Chang, Nanostructured high-entropy alloys with multiple principal elements: Novel alloy design concepts and outcomes, Adv. Eng. Mater. 6 (2004) 299–303. https://doi.org/10.1002/adem.200300567.

[30] D.G. Sangiovanni, W. Mellor, T. Harrington, K. Kaufmann, K. Vecchio, Enhancing plasticity in high-entropy refractory ceramics via tailoring valence electron concentration, Mater. Des. 209 (2021) 109932. https://doi.org/10.1016/j.matdes.2021.109932.

[31] J. Pötschke, M. Dahal, A. Vornberger, M. Herrmann, A. Michaelis, Production and properties of high entropy carbide based hardmetals, Metals (Basel). 11 (2021) 1–12. https://doi.org/10.3390/met11020271.

[32] X. Wang, T.G. Saunders, R. Sedlák, T. Csanádi, Y. Wang, J. Dusza, L. Fu, M.J. Reece, Synthesis and densification of (Zr-Hf-Nb-Ta)C-Co high entropy cermet prepared by pressureless melt infiltration using spark plasma sintering, J. Alloys Compd. 900 (2022). https://doi.org/10.1016/j.jallcom.2021.163412.

[33] J.O. Andersson, T. Helander, L. Höglund, P. Shi, B. Sundman, Thermo-Calc & DICTRA, computational tools for materials science, Calphad Comput. Coupling Phase Diagrams Thermochem. 26 (2002) 273–312. https://doi.org/10.1016/S0364-5916(02)00037-8.

[34] R.M. German, Powder metallurgy science, Metal Powder Industries Federation, 1994.

[35] B.D. Cullity, Elements of X-Ray diffraction, Second, Addison-Wesley Publishing Company Inc., 1978.

[36] A.R. Denton, N.W. Ashcroft, Vegard's law, Phys. Rev. A. 43 (1991) 3161–3164. https://doi.org/10.1103/PhysRevA.43.3161.

[37] M.D. Abràmoff, P.J. Magalhães, S.J. Ram, Image processing with imageJ, Biophotonics Int. 11 (2004) 36–41. https://doi.org/10.1201/9781420005615.ax4.

[38] C.S. Smith, L. Guttman, Measurement of Internal Boundaries in Three-Dimensional Structures By Random Sectioning, Jom. 5 (1953) 81–87. https://doi.org/10.1007/bf03397456.

[39] H.M. Rietveld, A profile refinement method for nuclear and magnetic structures, J. Appl. Crystallogr. 2 (1969) 65–71. https://doi.org/10.1107/s0021889869006558.

[40] D.K. Shetty, I.G. Wright, P.N. Mincer, A.H. Clauer, Indentation fracture of WC-Co cermets, J. Mater. Sci. 20 (1985) 1873–1882. https://doi.org/10.1007/BF00555296.

[41] W.C. Oliver, G.M. Pharr, An improved technique for determining hardness and elastic madulus using load and displacement, J Mater Res. 7 (1992) 1564–1583.

[42] H. Doi, Y. Fujiwara, K. Miyake, Y. Oosawa, A systematic investigation of elastic moduli

of Wc-Co alloys, Metall. Mater. Trans. 1 (1970) 1417–1425. https://doi.org/10.1007/BF02900264.

[43] X.X. Yu, G.B. Thompson, C.R. Weinberger, Influence of carbon vacancy formation on the elastic constants and hardening mechanisms in transition metal carbides, J. Eur. Ceram. Soc. 35 (2015) 95–103. https://doi.org/10.1016/j.jeurceramsoc.2014.08.021.

[44] M. HUMENIK, N.M. Parikh, Cermets: I, Fundamental Concepts Related to Micro-structure and Physical Properties of Cermet Systems, J. Am. Ceram. Soc. 39 (1956) 60–63. https://doi.org/10.1111/j.1151-2916.1956.tb15624.x.

[45] M. Labonne, J.M. Missiaen, S. Lay, A. Antoni-Zdziobek, O. Lavigne, L. Garcia, E. Tarrés, Sintering behavior, microstructure and mechanical properties of NbC-Ni alloys with different carbon contents, Int. J. Refract. Met. Hard Mater. 103 (2022). https://doi.org/10.1016/j.ijrmhm.2021.105771.

[46] M. Labonne, Sintering behaviour and microstructure evolution of NbC-Ni cemented carbides., Université Grenoble Alpes, 2020. http://tel.archives-ouvertes.fr/tel-03116918.

[47] L. Chen, W. Lengauer, K. Dreyer, Advances in modern nitrogen-containing hardmetals and cermets, Int. J. Refract. Met. Hard Mater. 18 (2000) 153–161. https://doi.org/10.1016/S0263-4368(00)00016-0.

[48] L. Chen, W. Lengauer, P. Ettmayer, K. Dreyer, H.W. Daub, D. Kassel, Fundamentals of liquid phase sintering for modern cermets and functionally graded cemented carbonitrides (FGCC), Int. J. Refract. Met. Hard Mater. 18 (2000) 307–322. https://doi.org/10.1016/S0263-4368(00)00041-X.

[49] P. Ettmayer, H. Kolaska, W. Lengauer, K. Dreyer, Ti (C, N) cermets metallurgy and properties, Int. J. Refract. Hard Mater. 13 (1995) 343–351. http://www.sciencedirect.com/science/article/pii/026343689500027G.

[50] J. Pötschke, M. Dahal, M. Herrmann, A. Vornberger, B. Matthey, A. Michaelis, Preparation of high entropy carbides by different sintering techniques, J. Mater. Sci. 56 (2021) 11237–11247. https://doi.org/10.1007/s10853-021-06004-y.

[51] S.Y. Ahn, S.W. Kim, S. Kang, Microstructure of Ti(CN)-WC-NbC-Ni Cermets, J. Am. Ceram. Soc. 84 (2001) 843–849. https://doi.org/10.1111/j.1151-2916.2001.tb00750.x.

[52] T. Csanádi, E. Castle, M.J. Reece, J. Dusza, Strength enhancement and slip behaviour of high-entropy carbide grains during micro-compression, Sci. Rep. 9 (2019) 1–14. https://doi.org/10.1038/s41598-019-46614-w.

[53] S.G. Huang, J. Vleugels, H. Mohrbacher, M. Woydt, Microstructure and tribological performance of NbC-Ni cermets modified by VC and Mo_2C, Int. J. Refract. Met. Hard Mater. 66 (2017) 188–197. https://doi.org/10.1016/j.ijrmhm.2017.03.012.

CRediT author statement

Zahid Anwer: Investigation, Validation, Software, Formal analysis, Visualization, Data curation and Writing – original draft.

Shuigen Huang: Conceptualization, Methodology, Supervision, Funding acquisition and Writing – review & editing.

Jozef Vleugels: Supervision, Resources and Writing – review & editing.

Declaration of interests

☒The authors declare that they have no known competing financial interests or personal relationships that could have appeared to influence the work reported in this paper.

☐The authors declare the following financial interests/personal relationships which may be considered as potential competing interests:

Highlights

- Fully dense (Ti,V,Nb,Ta,W)C-Ni cermets were prepared using conventional liquid phase sintering at 1420°C.
- The high entropy carbide phase formation was studied in detail at seven different temperatures and correlated with thermodynamic calculations.
- TaC and NbC hosted the other metal-carbide elements to form a single phase FCC high entropy carbide phase with ductile characteristics.